Ultramicroscopy 33 (1990) 27–39
North-Holland

ON THE CALCULATION OF ELECTRON MICROSCOPE IMAGES OF HOLES AND SPHERICAL INCLUSIONS USING THE MULTI-SLICE METHOD

K. SCHEERSCHMIDT and R. HILLEBRAND

Institute for Solid State Physics and Electron Microscopy of the Academy of Sciences of the GDR, Weinberg 2, DDR-4050 Halle/Saale, German Dem. Rep.

Received 26 February 1990

Dedicated to Professor Dr. Johannes Heydenreich on the occasion of his 60th birthday, also on behalf of Professor Dr. H. Bethge and Professor Dr. V. Schmidt

Electron microscope images are calculated to investigate the contrast of small cylindrical and wedge-shaped holes as well as of spherical inclusions with polynomial eigenstrains in gold films. The computer simulations are carried out by using the multi-slice method and by assuming a sandwich object structure having different hole diameters or atomic displacements within subsequent slabs. Diffraction contrast images of the defects – including image aberrations entirely – are compared with lattice fringe patterns and high-resolution electron micrographs (HREM) to evaluate the possibilities of interpreting the crystal defect fine structure. Particularly the variations in the contrast of the defects as well as the distortions in the lattice fringe and HREM patterns are correlated to both the defect nature and the imaging conditions, demonstrating the phase influence of the microscope aberrations.

1. Introduction

In previous papers [1–3] diffraction contrast images and lattice fringe patterns were computer-simulated to investigate the contrast effects and the optimum conditions of electron microscope imaging especially for small hexagonal dislocation loops and spherical inclusions. The method applied there consists in combining the calculation of diffraction contrast amplitudes with the Fourier transformation to include image aberrations. In addition, for spherical inclusions with polynomial eigenstrains the results were compared with analogous calculations using the multi-slice method. The outward or inward bendings of fringes caused by the defects were no longer found to unequivocally prove the defect nature. A comprehensive analysis of the fringe distortions in combination with a study of the black–white oscillations in diffraction contrast, however, should yield information on the local defect structure.

The lattice fringe distortions, i.e. shifting, bending and termination, are shown to be controlled by the phase differences between bright-field and dark-field amplitudes. With increasing resolution the influence of the elastic far-field of the defects in the micrographs is reduced and the contrast features are mainly determined by the central defect structure as well as by the imaging conditions. Therefore the fundamental features of the defect contrast are maintained even if the microscope aberrations are large; the fine details, however, are essentially influenced by through-focusing.

For studying the phase-influencing behaviour of the microscope in relation to the crystal defect fine contrast in detail, in this paper the image calculations of inclusions with polynomial eigenstrains are refined by using the multi-slice method. Varying the assumed inner structure of the spherical inclusion with an invariant and small far-field the calculations enable the discrimination to be made between imaging effects and contrast phenomena due to the defect fine structure.

Unlike the calculations for inclusions, multi-slice image simulations for holes, having circular cross sections but different border shapes, show

0304-3991/90/$03.50

similar but well distinguishable contrast effects. If no elastic displacements of the atoms in the matrix surrounding the hole are assumed, contrast fine structures arise due to Fresnel diffraction at the border between matrix and vacuum modified by the shape of the border (cylindrical, wedge- or crater-shaped). Especially for amorphous objects, Fresnel fringes occur as black–white contrast features parallel to the border which are used to correct the astigmatism and to align the focus conditions.

For crystals a striking effect occurs – called "spillover" in the following – with periodic lattice features obviously advancing across the border into the vacuum. The degree and perfection of this periodic continuation depend on the spatial and temporal coherence in the microscope. In refs. [4,5] the "spillover" is discussed as "lateral spread of lattice information into the region of the Fresnel fringes" applying the phase grating approximation. With the coherence not being explicitly considered, Fresnel fringes are utilized to calibrate the defocus in the HREM. Tanji and Cowley [6] studied the interaction of electron beams with an MgO surface. The interpretation of the experiments by computer simulation showed the sensitivity of the electron waves with respect to the out-of-crystal potential.

The "spillover" of the periodic lattice across the border of the hole has to be distinguished from the periodic continuation inherent in the numerical algorithm of the fast Fourier transform of the multi-slice simulation procedure. The latter produces virtual contrast features at the boundary of the supercells due to the aliasing and truncation of the finite Fourier transform. Due to the referred investigation of holes instead of borders at half-infinite crystals the virtual effects of aliasing and truncation decrease.

The calculation of bright-field (BF) and dark-field (DF) diffraction contrast images with lattice fringe patterns (LF) as well as of high-resolution micrographs (HREM) can be carried out by the multi-slice method by using appropriate imaging parameters and by varying the position of the objective aperture. Applying the different imaging modes to compare the contrast effects for small inclusions with those for holes enables one to assess the possibilities of interpreting the crystal defect fine structure with respect to the lateral spread of lattice information due to the microscope aberrations.

2. Method of computer simulation

The HREM micrographs were calculated by using a modified multi-slice program [7,8] with both discrete Fourier transform and convolution (128×128 pixels). Without discrete real-space sampling the Fourier transform of the projected potential of each slice is directly evaluated from the atomic coordinates of the structure model and the associated atomic scattering amplitude. For a sufficient accuracy in applying the method to crystals containing lattice defects with a non-vanishing elastic far-field the lateral extension of supercells should be dimensioned to avoid effects of aliasing and truncation.

Fulfilling these numerical requirements, the specimen model for the multi-slice calculations is based on a gold unit cell, which is transformed into (110) direction and is multiplied by 6 and 9, respectively, for the new axes within the transformed unit mesh. In (110) projection the face-centered cubic unit cell with a lattice constant of 0.4079 nm shows a mesh of 0.5768×0.4079 nm^2 and a slice thickness of $\Delta z = 0.2884$ nm. The supercell of 6×9-Au(110) thus yields an extension by 3.461×3.671 nm^2, containing 216 atoms, whereas the slice thickness does not change. The specimen model for the multi-slice calculations is constructed by a variable sequence of perfect and differently distorted crystal slices in the form of a sandwich structure. The distorted slabs are generated thus modifying the perfect supercells either by removing atoms to produce holes or by displacing atoms according to the elastic strains to describe inclusions.

For calculating the image contrast of inclusions the atoms of the 6×9-Au(110) supercells are displaced according to the eigenstrains of the extended Ashby–Brown precipitate given in eq. (10) of ref. [3]. The elastic displacement field reads

$$\boldsymbol{u}(\boldsymbol{r}) = \begin{cases} \epsilon \boldsymbol{r} (R_0/r)^3 & \text{for } r \geq R_c, \\ \epsilon \boldsymbol{r} \left[a \ln(r/R_0) + \sum_{j \geq -3} b_j (r/R_0)^j \right] & \\ & \text{for } r \leq R_c, \end{cases} \quad (1)$$

with the defect radius R_0, the constrained strain ϵ, and the characteristic constants R_c, a and b_j of the polynomial displacements. For $R_c = R_0$, $a = 0$, $b_j = 0$, besides $b_0 = 1$ the displacements are reduced to that of an Ashby–Brown precipitate, for $R_c \approx 0$ or $b_{-3} = 1$ but $a = 0$, $b_j = 0$ the displacements are those of pure dilation or compression centre. The displacements (1) are continuous for $r = R_c$ if the additional condition,

$$(R_0/R_c)^3 = a \ln(R_c/R_0) + \sum_{j \geq -3} b_j (R_c/R_0)^j, \quad (2)$$

is fulfilled.

Otherwise, if condition (2) is not maintained the additional jump $\boldsymbol{u}(\boldsymbol{r})$ for $r = R_c$ can be interpreted as sliding inclusion or incoherent precipitate.

The general spherical inclusion with continuous displacements described by eqs. (1) and (2) has a far-field of Ashby–Brown type out of $r \geq R_c$, representing polynomial eigenstrains within $r \leq R_c$. The strength of the field is determined by ϵR_0^3, with $\epsilon > 0$ characterizing dilation-type defects (interstitials) and $\epsilon < 0$ compression ones (vacancies).

For the assumed size and strength of the defect ($R_0 = 1.6$ nm, $\epsilon = 0.05$) the local displacements of the atoms are almost vanishing near the lateral cell boundaries to fulfill the conditions of periodic continuation. Five different model slices of $\Delta z = 0.288$ nm in thickness are sufficient to approximate the defect structure parallel to the beam direction. The defect slices are disturbed according to eq. (1) as a function of the distance from the defect centre $\boldsymbol{r} - \boldsymbol{r}_0$, and embedded in perfect slices. Fig. 1 schematically shows the displacements of a pure dilation centre in inclined parallel view of the disturbed 6×9-Au(110) supercells. Fig. 1a gives the perfect cell for comparison; figs. 1b–1f show the cells with distances $z - z_0 = -0.576$, -0.288, 0, 0.288 and 0.576 nm between the centres of cells and the inclusion, respectively. Atoms which are absent in the projections are at greater distances from the border of the cell.

For simulating objects containing holes five differently distorted slices are established, each of

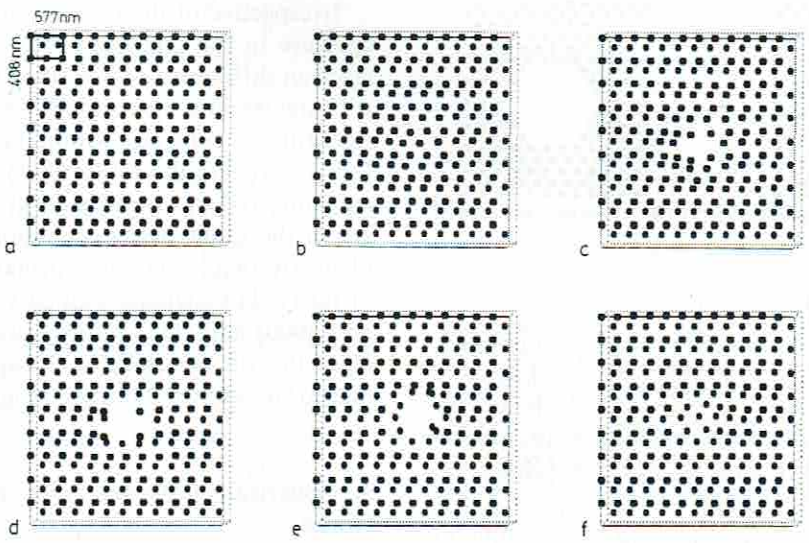

Fig. 1. Inclined (110)-parallel view of the perfect (a) and distorted (b–f) 6×9-Au(110) slices for a sandwich object used in multi-slice image calculations of gold foils containing inclusions. Distance between centres of the slices and the inclusion: $z - z_0 = -2\,\Delta z$ (b), $-\Delta z$ (c), 0 (d), Δz (e), $2\,\Delta z$ (f); slice thickness $\Delta z = 0.288$ nm, radius of the inclusion $R_0 = 1.6$ nm, atomic displacements of a pure dilation centre $\epsilon = 0.05$.

which corresponds to a perfect supercell having a cylindrical hole. The diameters used are $2R_0 =$ 0.78, 0.88, 1.26, 1.44 and 1.72 nm, i.e. around the middle of the supercell 8, 14, 24, 30 and 42 atoms are removed, respectively. Varying combinations of these slices enables one to investigate holes of different structures in beam direction. Fig. 2 schematically shows the (110) projections of two generated slabs whose hole diameters are $2R_0 =$ 0.88 nm in (a) and $2R_0 = 1.44$ nm in (b). Furthermore, the different sandwich structures used for the image simulations are presented in figs. 2c–2e corresponding to a parallel-sided cylindrical hole, a double-wedge-shaped and a crater-shaped one, respectively. Image calculations of thin objects containing holes with their diameters decreasing from top to bottom of the foil (cf. fig. 2e) have not revealed remarkable differences from respective calculations with the diameters increasing in beam direction. Thus the investigations are restricted to the above three cases schematically shown, which can be discriminated by the image contrast.

The multi-slice recursion was carried out by including approximately 7000 beams for accelerating voltages of $V = 100$ or 400 kV. For the contrast transfer function a lens aberration of $C_s = 1$ mm is assumed, preferring the Gauss defocus ($\Delta = 0$) or the Scherzer defocus ($\Delta = 48$ nm for 400 kV, $\Delta = 62$ nm for 100 kV). The coherence conditions are varied by choosing a defocus spread of $2 \leq \delta f \leq 5$ nm and assuming the angular divergence of the incident beam in the range of $0.5 \leq \alpha_B \leq 1.5$ mrad. The microscope imaging conditions are adjusted by the position and diameter $\alpha(hkl)$ of the aperture in the plane of the diffraction pattern. Thus, for bright-field (BF) diffraction contrast the aperture $\alpha(000)$ is centered at the transmitted beam (000) and chosen smaller than the reciprocal 111-lattice distance $\alpha(000) = 2.1$ nm^{-1}. For the dark-field (DF) diffraction contrast the beam considered is tilted into the optical axis of the microscope and the aperture $\alpha(\bar{1}1\bar{1}) = 2.1$ nm^{-1} is placed around it. Two-beam lattice fringes (LF) are calculated using a displaced aperture in the middle between (000) and $(\bar{1}1\bar{1})$ with the diameter being larger than the 111-reciprocal lattice vector $\alpha(\bar{1}/2, 1/2, \bar{1}/2) = 2.5$ nm^{-1}. Three-beam lattice fringes (3B) are calculated with $\alpha(\bar{5}/6, 5/6, 0) = 3$ nm^{-1} including (000), $(\bar{1}1\bar{1})$ and $(\bar{1}11)$ reflexes, whereas high-resolution micrographs are simulated with $\alpha(000) = 5$ nm^{-1} including all beams up to (002).

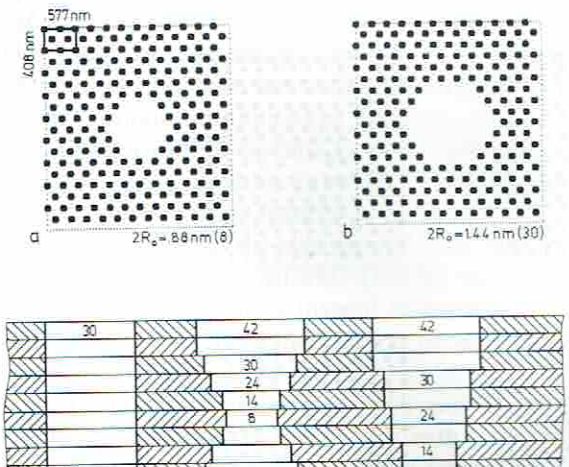

Fig. 2. Schematic drawing of sandwich objects for multi-slice calculations of gold foils with holes: (110) projection of 6×9-Au(110) slices with diameters $2R_0 = 0.88$ nm (a), 1.44 nm (b); slice sequences of a parallel-sided cylindrical hole (c), double-wedge-shaped (d) and crater-shaped (e) hole.

Irrespective of the position and diameter of the aperture in the imaging process the excitation in electron diffraction is described by the pole vector $\boldsymbol{p}$ characterizing the incident beam with respect to the Brillouin zone axis within the diffraction plane. For $\boldsymbol{p} = \frac{1}{2}(hkl)$ the reflex (hkl) and all the corresponding reflexes positioned at the Ewald sphere are in the exact Bragg excitation. The simulation of nearly two-beam cases demands the excitation of the $(\bar{1}1\bar{1})$ systematic row in such a manner that only (000) and $(\bar{1}1\bar{1})$ reflexes are strongly excited. Here the tilt $\boldsymbol{p} = \frac{1}{4}(7, \bar{7}, \bar{20})$, approximately normal to the excited $\bar{1}1\bar{1}$ row, is applied.

3. Spherical inclusions with polynomial eigenstrains

Figs. 3 and 4 show calculated BF, DF, LF and 3B patterns of spherical inclusions according to eqs. (1) and (2) for different polynomial eigen-

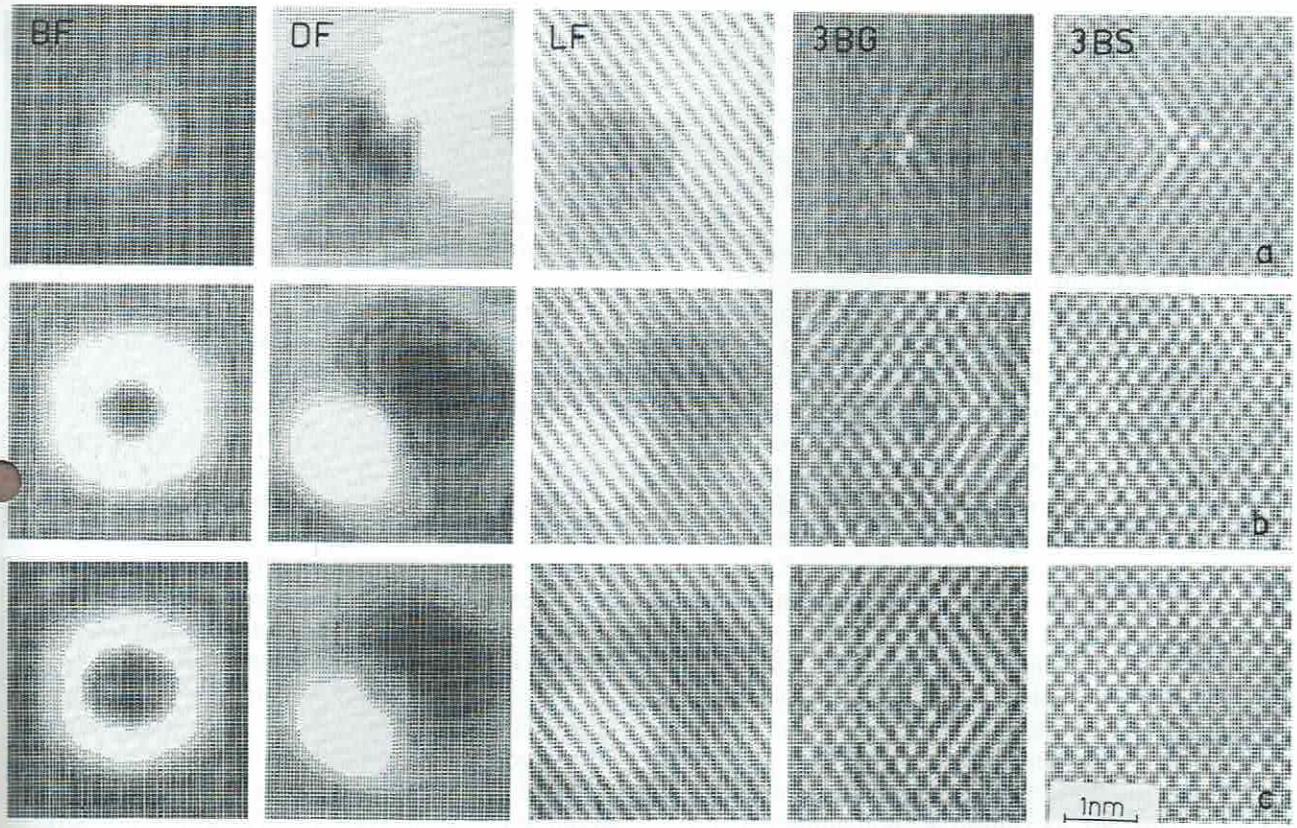

Fig. 3. Multi-slice image calculations of spherical inclusions with different polynomial defect eigenstrains ($R_c = 0$, $a = 0$, $b_{-3} = 1$ (a); $R_c = 1.2\ R_0$, $a = 16.4$, $b_2 = -0.5$ (b); $R_c = R_0$, $a = 20.0$, $b_{-2} = 1$ (c)) and different imaging conditions (BF: $\Delta = 0$, $\alpha(000) = 2.1$ nm^{-1}; DF: $\Delta = 0$, $\alpha(\bar{1}\bar{1}\bar{1}) = 2.1$ nm^{-1}; LF: $\Delta = 0$, $\alpha(\bar{1}/2, 1/2, \bar{1}/2) = 2.5$ nm^{-1}; 3BG: $\Delta = 0$, $\alpha(\bar{5}/6, 5/6, 0) = 3$ nm^{-1}; 3BS: $\Delta = 62$ nm, $\alpha(\bar{5}/6, 5/6, 0) = 3$ nm^{-1}). Parameters: $V = 100$ kV, $C_s = 1$ mm, $\boldsymbol{e} = [110]$, $R_0 = 1.6$ nm, $\epsilon = 0.05$, $t = 21\ \Delta z$, $\Delta z = 0.288$ nm, $\boldsymbol{p} = (000)$.

strains. While in fig. 3 the beam is chosen in close-symmetrical incidence $\boldsymbol{e} = [110]$ with $\boldsymbol{p} = [000]$, in fig. 4 the tilt is used of $\boldsymbol{p} = \frac{1}{4}(7, \bar{7}, \overline{20})$ with respect to the [110] Brillouin zone axis. Thus, in fig. 4 the $(\bar{1}\bar{1}\bar{1})$ reflex and no other strong reflex of the perfect Au lattice is in the very Bragg excitation. The imaging conditions for the BF, DF and LF patterns are those given in section 2, i.e. $V = 100$ kV, $C_s = 1$ mm, $\Delta = 0$, $\alpha(000) = 2.1$ nm^{-1} (for BF), $\alpha(\bar{1}\bar{1}\bar{1}) = 2.1$ nm^{-1} (for DF), and $\alpha(\bar{1}/2, 1/2, \bar{1}/2) = 2.5$ nm^{-1} (LF). Both the different 3B patterns are calculated in the Gauss focus ($\Delta = 0$, 3BG) and in the Scherzer focus ($\Delta = 62$ nm, 3BS) with $\alpha(000) = 3$ nm^{-1}. In figs. 3a and 4a the inclusion ($R_0 = 1.6$ nm, $\epsilon = 0.05$) is assumed to be a pure dilation centre ($R_c = 0$, $a = 0$, $b_{-3} = 1$, $b_j = 0$). Figs. 3b and 4b demonstrate the case of polynomial eigenstrain with a quadratic term and a compensating logarithmic one ($R_c = 1.2 R_0$, $a = 16.4$, $b_{+2} = -5$, $b_j = 0$), whereas in figs. 3c and 4c a $1/r^2$ dependence is chosen ($R_c = R_0$, $a = 20.0$, $b_{-2} = 1$, $b_j = 0$). In all cases the foil thickness is $t = 21\ \Delta z \approx 6$ nm, the depth position is $t_0 = t/2$.

The displacements used for the multi-slice calculations of figs. 3 and 4 are schematically drawn in fig. 5. The curves in fig. 5 give the amount of the displacements which are spherically symmetrical, fig. 5a represents the pure dilation centre, whereas (b) and (c) show the quadratic and $1/r^2$ dependences, respectively. For the comparison with the calculations of the previous paper [3],

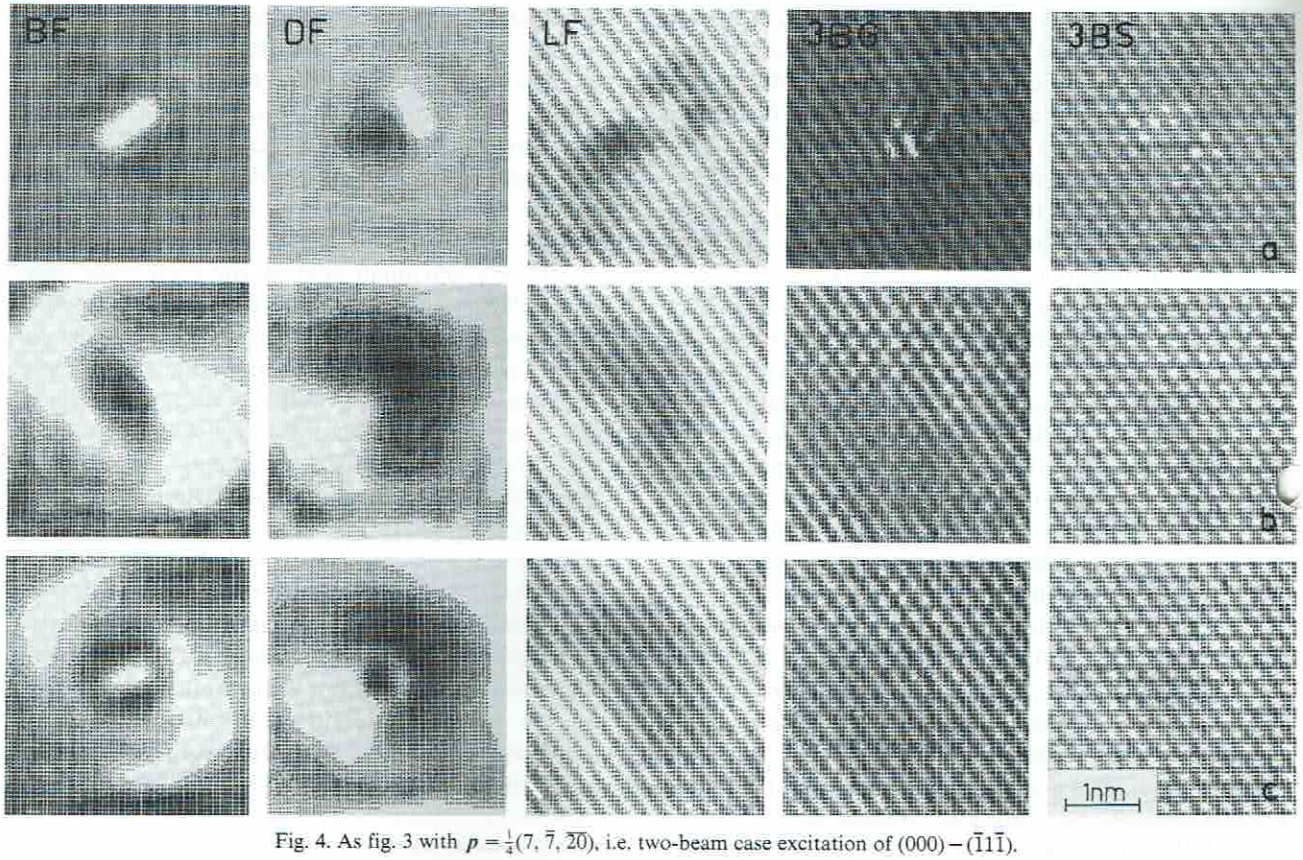

Fig. 4. As fig. 3 with $\boldsymbol{p} = \frac{1}{4}(7, \bar{7}, \bar{2}0)$, i.e. two-beam case excitation of $(000) - (\bar{1}1\bar{1})$.

curve (d) in addition displays the eigenstrains with vanishing stresses. The distance between the perpendicular dashed lines in fig. 5 represents the slice thickness used in the multi-slice calculations. The small changes of the displacement field outside the five slices applied for the defect description can be neglected in the computations.

For the sake of simplicity and as the contrast is not sensitive to small parameter changes the three cases of figs. 3 and 4 are chosen exactly fulfilling

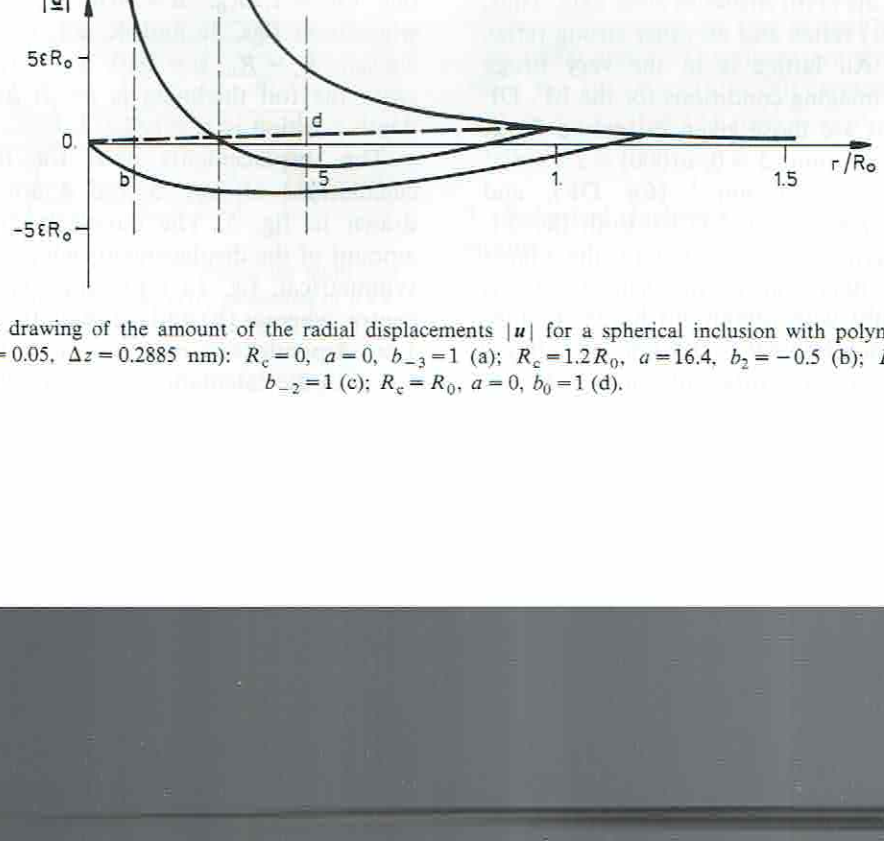

Fig. 5. Schematic drawing of the amount of the radial displacements $|\boldsymbol{u}|$ for a spherical inclusion with polynomial eigenstrains ($R_0 = 1.6$ nm, $\epsilon = 0.05$, $\Delta z = 0.2885$ nm): $R_c = 0$, $a = 0$, $b_{-3} = 1$ (a); $R_c = 1.2R_0$, $a = 16.4$, $b_2 = -0.5$ (b); $R_c = R_0$, $a = 20.0$, $b_{-2} = 1$ (c); $R_c = R_0$, $a = 0$, $b_0 = 1$ (d).

condition (2) to avoid a sliding inclusion. To guarantee a stress-free surface of the inclusion another condition has to be fulfilled, which has not yet explicitly been discussed and means $\mu(R_c) = 0$ at the surface of the inclusion for the body density μ introduced in eq. (6) of ref. [3]. This additional condition is only approximately satisfied here for cases (b) to (d). The different polynomial eigenstrains characterize different energy contents of the inclusion; suppressing terms of r^{-3} and r^{-2}, i.e. $b_{-3} = b_{-2} = 0$, yield non-singular defects. The contrast effects discussed in the following allow one to discriminate singular displacement fields from non-singular ones but they do not seem sensitive enough to allow a sufficient discrimination between, for instance, cases (b) to (d).

The bright-field contrast (BF) for central incidence (fig. 3) is centro-symmetric; the tilted object (fig. 4) generates black–white contrast features of two-fold symmetry. Here, the pure dilation centre produces a bright spot-like contrast within the dark background, whereas due to the alternating displacement field in (b) and (c) a ring-shaped contrast may be expected. In the dark-field diffraction contrast (DF) always black–white figures occur with the black–white vector being either antiparallel (figs. 3a, 4a) or parallel to the excited diffraction reflex. The uniform contrast shows a small number of fine details only for central incidence as well as for the pure dilation centre and for tilting. In the lattice fringe patterns the black–white features according to the DF are maintained in the background. The most significant fringe distortions are detected in fig. 3b.

The relatively strong displacement gradient of the pure dilation centre prevents the satisfactory visualization of the lattice fringes in the 3-beam images. Because of the asymmetrical imaging conditions, the defect appears as an asymmetric arrangement of bright dots. Unlike this, cases (b) and (c) of figs. 3 and 4 better visualize the lattice fringes and the atomic columns, respectively. Thus the defects occur as brighter spots in the Gauss focus and as darker ones under the Scherzer imaging condition. The borders of the defects are strongly facetted. For the tilted crystalline specimen containing the inclusion (fig. 4, 3B cases) the computation does not provide locally specific contrast features.

4. Influence of microscope aberrations on the HREM imaging of holes

Perforated gold films with well defined holes and lattice defects can be produced by vacuum deposition on specially prepared substrates of sodium chloride, starting from epitaxial islands of gold being well preoriented by a pulsed arc deposition technique and generating the defects due to the incomplete coalescence of islands [9]. Fig. 6 presents experimental BF diffraction contrast micrographs (a, b) and LF patterns (c, d) showing an [001]-oriented gold film of an average thickness of about 12 nm and containing holes. Annealing the gold film in vacuum for 110 min at 280 °C (see fig. 6b) causes the holes of the as-deposited film of fig. 6a to shrink or to grow. In the places of small holes (see arrow) mobile dislocations will occur indicating a closure failure of the crystal lattice around the hole. Figs. 6c and 6d show {200} lattice fringe micrographs (JEM100C at 100 kV, tilted illumination, 4 beams) of the small holes indicated by arrows in fig. 6a after some minutes of electron irradiation [10]; here the lattice mismatch is also obvious and the additional contrast fringes are characterized by dislocation symbols. Around the holes in the BF images one or two thickness extinction contours occur which depend on the different excitation conditions of figs. 6a and 6b, respectively. The position of the thickness contours slightly asymmetric with respect to the border indicates an inclination angle varying with the azimuth; weak-beam images, not shown here, proved a steep descent of the border for the approximately double-wedge-shaped holes. Owing to the imaging conditions Fresnel fringes are suppressed in the BF contrast. In figs. 6c and 6d the LF patterns show lattice fringes within the border of the hole which either arise from the transport of the material due to the electron irradiation, or which have to be interpreted as a virtual effect due to image aberrations. As to investigating whether the imaging process can generate virtual LF patterns of such a kind, in the following calculations

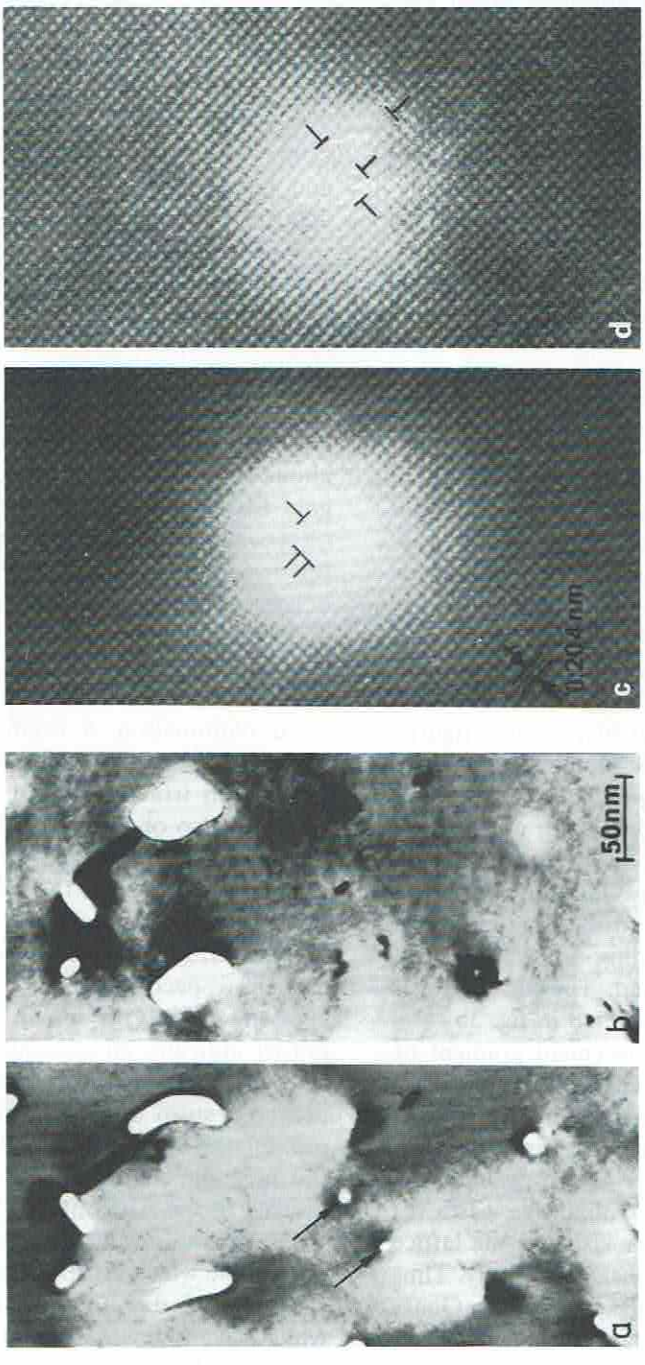

Fig. 6. Perforated (001) gold films of about 12 nm in thickness in 100 kV bright-field (a, b) and lattice-fringe (c, d) contrast [9,10]: as-deposited (a), vacuum-annealing at 280 °C for 120 min (b), holes indicated in (a) after electron irradiation (c, d).

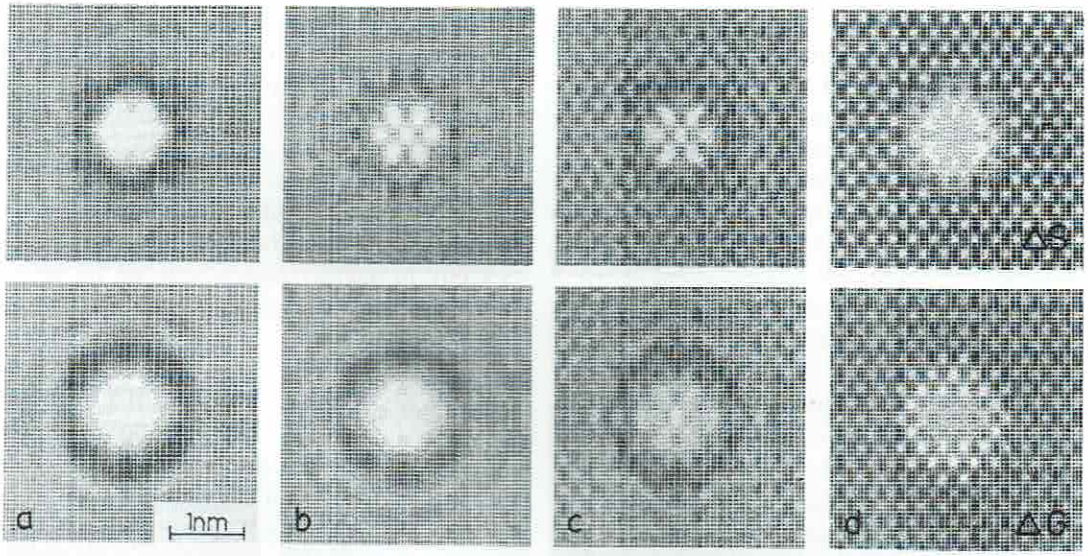

Fig. 7. HREM contrast simulations of double-wedge-shaped holes in 6×9-Au(110) cells ($N=11$, $\Delta z=0.288$ nm, $\Delta_G=0$). (a) $\delta f=5$ nm, $\alpha_B=1.5$ mrad; (b) $\delta f=2$ nm, $\alpha_B=1.5$ mrad; (c) $\delta f=2$ nm, $\alpha_B=0.5$ mrad; (d) $\delta f=5$ nm, $\alpha_B=0.5$ mrad; (a–c) $V=100$ kV, $C_s=1$ mm, $\Delta_S=62$ nm, $\alpha=5$ nm^{-1}; (d) $V=400$ kV, $C_s=1$ mm, $\Delta_S=48$ nm, $\alpha=7.5$ nm^{-1}.

are discussed of contrast effects at holes in (110)-gold films for the simplified model objects as referred to in section 2. A subsequent paper is under preparation taking into account the exact experimental parameters.

Different hole profiles (double-wedge-shaped, parallel-sided cylinder, crater-shaped) are modelled by an appropriate slice sequence of 6 × 9-Au(110) cells with a varying number of atoms inside a cylindrical region being removed (for de-

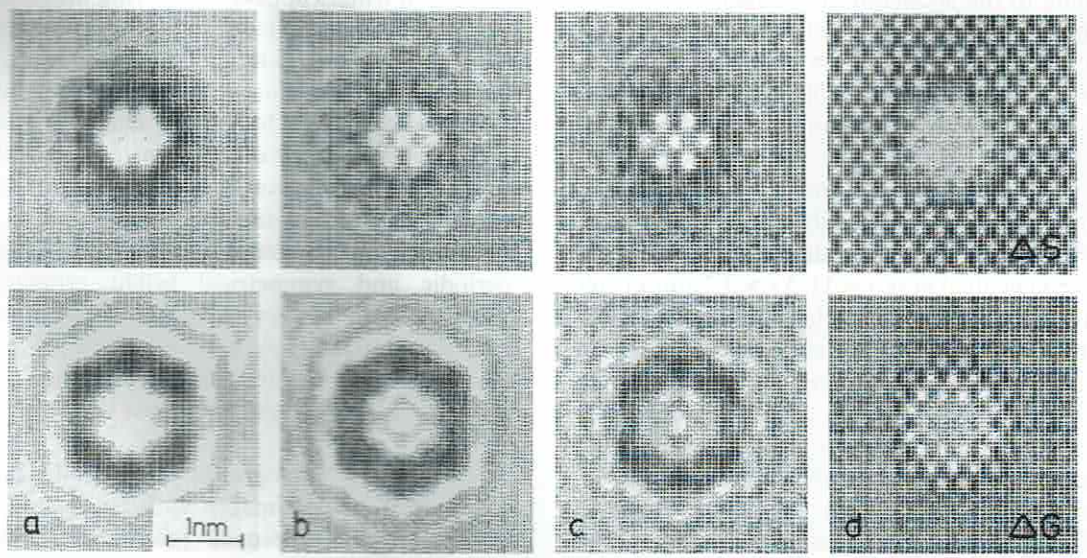

Fig. 8. HREM contrast simulations of double-wedge-shaped holes in 6×9-Au(110) cells ($N=14$, $\Delta z=0.288$ nm, $\Delta_G=0$). (a) $\delta f=5$ nm, $\alpha_B=1.5$ mrad; (b) $\delta f=2$ nm, $\alpha_B=1.5$ mrad; (c) $\delta f=2$ nm, $\alpha_B=0.5$ mrad; (d) $\delta f=5$ nm, $\alpha_B=0.5$ mrad; (a–c) $V=100$ kV, $C_s=1$ mm, $\Delta_S=62$ nm, $\alpha=5$ nm^{-1}; (d) $V=400$ kV, $C_s=1$ mm, $\Delta_S=48$ nm, $\alpha=7.5$ nm^{-1}.

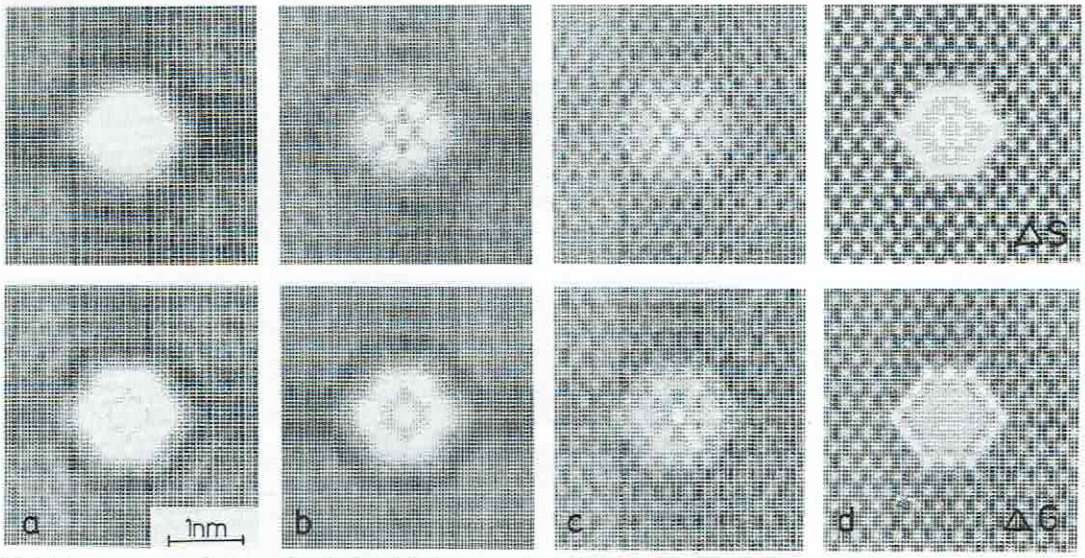

Fig. 9. HREM contrast simulations of cylindrical holes in 6×9-Au(110) cells (N = 11, $\Delta z = 0.288$ nm, $\Delta_G = 0$). (a) $\delta f = 5$ nm, $\alpha_B = 1.5$ mrad; (b) $\delta f = 2$ nm, $\alpha_B = 1.5$ mrad; (c) $\delta f = 2$ nm, $\alpha_B = 0.5$ mrad; (d) $\delta f = 5$ nm, $\alpha_B = 0.5$ mrad; (a–c) $V = 100$ kV, $C_s = 1$ mm, $\Delta_S = 62$ nm, $\alpha = 5$ nm^{-1}; (d) $V = 400$ kV, $C_s = 1$ mm, $\Delta_S = 48$ nm, $\alpha = 7.5$ nm^{-1}.

tails see section 2). In figs. 7–9 image simulations are discussed of double-wedge-shaped and cylindrical holes. For accelerating voltages of $V = 100$ and 400 kV the coherence and the defocus are varied (Gauss focus $\Delta = 0$ and Scherzer focus according to the acceleration voltage). The figures demonstrate the possibility of discriminating different shapes and sizes of the holes analyzing the contrast as well as the "spillover" of the fringe patterns into the inner region of the hole – depending on the coherence.

The slice sequence, assumed for the contrast calculations in fig. 7, describes a double-wedge-shaped hole. For an accelerating voltage of 100 kV the specimen thickness $t = 11\ \Delta z \approx 3.2$ nm corresponds to $\frac{3}{4}\xi_0$ (ξ_0 = extinction distance of 000-beam) for the central Laue case; for $V = 400$ kV the extinction distance increases and $t = 11\ \Delta z$ corresponds with $\xi_0/2$. The degree of coherence, which is determined by the defocus spread δf (chromatic aberration) and the illumination aperture α_B (spatial coherence), is varied so as to comprehensively study the resolution and periodic continuation. In the right columns (d) of figs. 7 to 9 standard characteristics of a medium-voltage HREM device ($V = 400$ kV, $C_s = 1$ mm, $\delta f = 5$ nm, $\alpha_B = 0.5$ mrad) are assumed. In the calculated micrographs the hole in the crystal is imaged as a bright area. For a specimen thickness of $\xi_0/2$, which corresponds to a diameter of 1.5 nm between the hole edges in the model (cf. fig. 2), dark extinction fringes appear. Improving the coherence (see figure captions) of the 100 kV microscope ($\delta f = 5$ nm, $\alpha_B = 1.5$ mrad (a) to $\delta f = 2$ nm, $\alpha_B = 0.5$ mrad (b)) will cause a fine structure within the hole region. While for a low coherence (a) the defocus dependence of the contrast is weak, for (b) and (c) the Scherzer focus ($\Delta = 62$ nm) and the Gaussian focus provide different "in-hole" structures. For the Scherzer focus (top) of (b) and (c) periodic and symmetrical bright arrangements arise, but they do not reproduce the distances of the gold lattice. They are influenced by the defocus, i.e. by the contrast transfer function, as well as by the wedge-shaped border of the hole (cf. fig. 9).

The 400 kV micrographs clearly show that the gold lattice can be imaged with reversed contrast because of the improved resolution. Compared with the bulk, the wedge region of the hole appears brightened, especially for $\Delta = 0$. The central hole area is not structured; the point resolution

and the reduced oscillations of the CTF for 400 kV obviously allow one to differentiate between the bulk contrast, the wedge contrast and the "in-hole" signal.

In fig. 8 the computations, discussed above, are carried out for an increased crystal thickness ($t = 14\,\Delta z \approx 4$ nm, i.e. $t = \xi_0$ for $V = 100$ kV and $t = \frac{3}{4}\xi_0$ for $V = 400$ kV) under identical imaging conditions. At an accelerating voltage of 100 kV the dark $\xi_0/2$ rings are surrounded by bright extinction fringes for $t = \xi_0$ (see $\Delta = 0$ in figs. 8a–8c). Because of contrast normalization applied here the bulk lattice is not visible in the images. The "in-hole" interference patterns ($\Delta = 62$ nm (b, c)) are comparable to those of fig. 7.

The 400 kV micrograph in the Scherzer focus exhibits a very good contrast of the perfect gold lattice, whereas the hole and the wedge-shaped region are more or less unstructured. For $\Delta = 0$ no bulk contrast is formed, but the decreasing specimen thickness at the inclined hole border provides patterns that are interpretable in terms of the interatomic distances.

A cylindrical hole may be modelled, if the three-dimensional specimen applied to the contrast simulations is built up of identical slices of the described 6×9-Au(110) type (see fig. 2). The diameter of the hole, assumed in fig. 9, is $2R_0 = 1.44$ nm; it is oriented parallel to the electron beam. Perpendicular crystal borders improve the possibility of distinguishing effects of the specimen thickness (extinction contrast) from those of the imaging system (contrast transfer). In general, the holes appear bright in the HREM micrographs. The dark fringes of the wedge-shaped holes in figs. 7 and 8, typical of $t = \xi_0/2$, are fading.

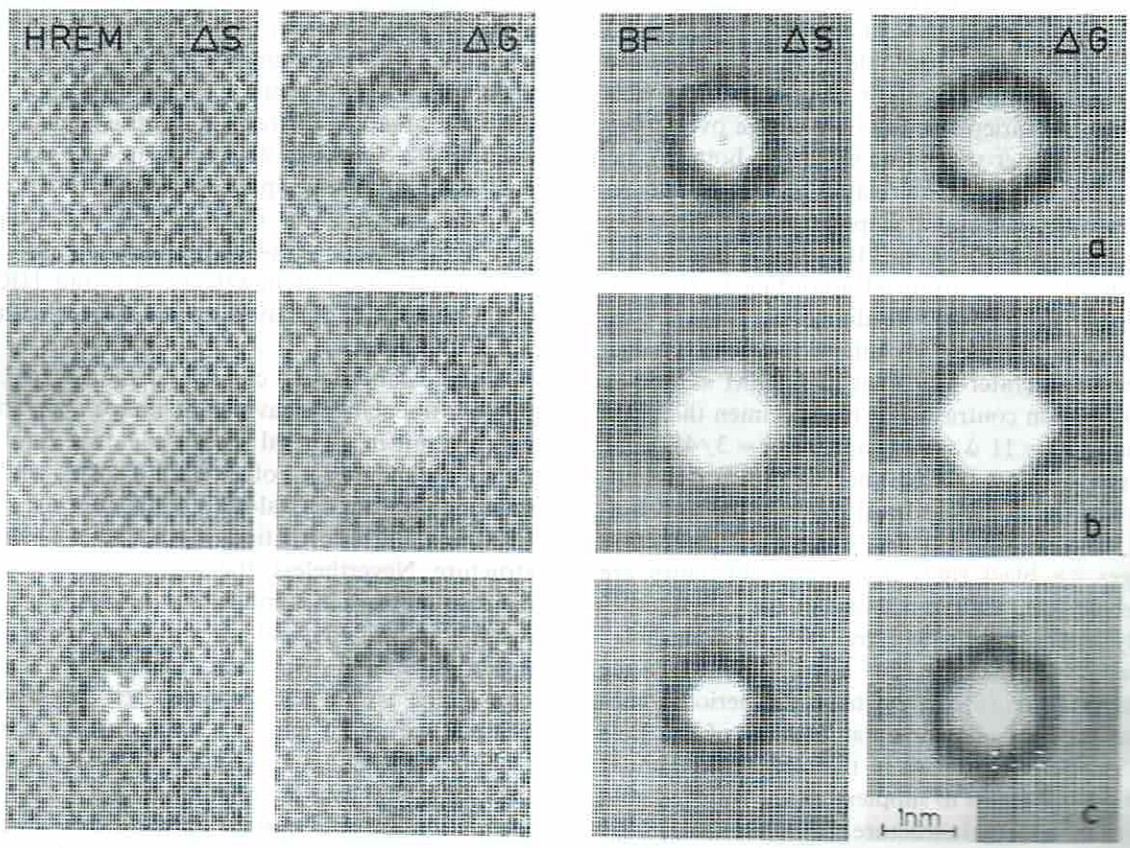

Fig. 10. HREM contrast simulations of holes in 6×9-Au(110) cells with different hole profiles: double-wedge-shaped (a), cylindrical (b), crater-shaped (c). Parameters: $N = 11$, $\Delta z = 0.288$ nm; $V = 100$ kV, $C_s = 1$ mm, $\delta f = 2$ nm, $\alpha_B = 0.5$ mrad, $\Delta_2 = 62$ nm, $\Delta_1 = 0$. HREM: $\alpha = 5$ nm^{-1}, BF: $\alpha = 2.1$ nm^{-1}

The other contrast features of the 100 kV patterns are more or less maintained, excluding the hole contrast for a very high coherence (fig. 8c: $\delta f = 2$ nm, $\alpha_B = 0.5$ mrad). The crystal lattice seems to continue in the central hole region. The correct interatomic distances are reproduced for the Scherzer focus.

In the 400 kV patterns of fig. 9 the gold lattice is clearly resolved. The periodic continuation, typical of the strongly oscillating 100 kV contrast transfer function for a high coherence, is not observed. The increased point resolution and the specific damping envelope prevent inner-hole pseudo-structures from occurring.

Multi-slice simulations of electron microscope images on the basis of extended pseudo-cells with defects enable a wide range of resolution to be studied, including also the diffraction contrast technique. In fig. 10 HREM images ($\alpha(000) = 5$ nm^{-1}), and the bright-field contrast ($\alpha(000) = 2.1$ nm^{-1}) of three different hole models are discussed for an accelerating voltage of 100 kV. The hole profiles are varied from double-wedge over cylindrical- to crater-shaped ones (top to bottom), i.e. the upper two rows are related to figs. 7c and 9c, respectively. The crater-shaped model of the above described set of 6×9-Au(110) slices is established, but the slices are arranged according to the continuously decreasing hole diameter. There are no significant contrast variations between wedge-shaped and crater-like holes in HREM as well as in diffraction contrast. For the specimen thickness assumed ($t = 11\ \Delta z = 3.2$ nm, i.e. $t = 3/4\xi_0$) the projection effect of EM imaging is still dominating. For the non-cylindrical models (top and bottom row of fig. 10) the dark $\xi_0/2$ extinction fringes, e.g. black rings around a bright centre, are observed for a wide range of defocus values, especially in the bright-field contrast. The "in-hole" patterns of the HREM micrographs for the Scherzer focus (a) demonstrate the periodic continuation. For perpendicular borders of the hole this interference process in the brightened circular background seems to supplement the resolved gold lattice by a virtual structure.

The contrast phenomenon of Fresnel fringes parallel to and outside the border of amorphous HREM specimens is modified here. While for quasi-continuous amorphous objects the contrast transfer function more or less exclusively determines the image within the coherence limitations, for crystalline samples the periodicity "spills over" into the vacuum. The point spread function, which is the real-space Fourier transform of the CTF, transfers the lattice information into the space out of the crystal. The up-to-date 400 kV high-resolution microscopes damp the effect of periodic continuation, because the improved transfer characteristic reduces the aberrations of the $1/d$ spectrum to be resolved.

5. Conclusions

Contrast simulations using the multi-slice algorithm are carried out to investigate electron microscope imaging of spherical inclusions with polynomial eigenstrains as well as of gold films containing holes. According to the imaging conditions, e.g. size and position of the objective aperture, BF and DF diffraction contrast images are studied and compared with calculated LF patterns and HREM micrographs. While the diffraction contrast images show more or less unstructured and symmetrical spot-like patterns in BF and black–white features in DF, the LF and HREM images generally display distorted fringes with residual DF contrast.

The calculations clearly demonstrate the phase-influencing behaviour of image aberrations which result in a lateral spread of lattice information into the region of Fresnel fringes, and its influence on the crystal-defect fine contrast overwhelming the information about the local defect structure. Nevertheless, the analysis of diffraction contrast features in combination with lattice fringe distortions should yield information on the local defect structure; especially the different polynomial eigenstrains can be correlated directly with contrast variations and the fringe modifications.

For small circular holes the contrast of extinction contours can be related to the shape and inclination of the border of the holes. Fresnel fringes, being undistorted black–white fringes at amorphous specimen boundaries, are modified in crystal structure imaging. The influence of the

varying coherence on the visual spread of the crystalline periodicity and the amount is significant for the Scherzer focus as well as for the Gauss focus. Assuming a high coherence the "in-hole" periodic continuation for 200 kV can be correlated to the strongly oscillating contrast transfer function. For the 400 kV HREM the "in-hole" contrast is more or less unstructured because of the improved point resolution. Neglecting the electron optical aberrations in the computer simulations clearly proved the mechanism of the spread of the lattice information, i.e. the "spillover" of the periodic patterns into the out-of-crystal regions is not caused by the electron diffraction process but by the microscopical aberrations.

References

[1] K. Scheerschmidt and R. Hillebrand, Phys. Status Solidi (a) 91 (1985) 465.
[2] R. Hillebrand, K. Scheerschmidt and J. Heydenreich, Ultramicroscopy 20 (1986) 279.
[3] K. Scheerschmidt, R. Hillebrand and J. Heydenreich, Phys. Status Solidi (a) 116 (1989) 123.
[4] A.R. Wilson, L.A. Bursill and A.E.C. Spargo, Optik 52 (1978/79) 313.
[5] A.R. Wilson and A.E.C. Spargo, Optik 63 (1982) 1.
[6] T. Tanji and J.M. Cowley, Ultramicroscopy 17 (1985) 287.
[7] A.J. Skarnulis, Thesis, Arizona State University, 1975.
[8] R. Hillebrand, Thesis, Universität Halle, 1987.
[9] R. Scholz and C.L. Bauer, Scripta Met. 18 (1984) 411.
[10] R. Scholz, private communication.